Rheological and structural studies of linear polyethylene melts under planar elongational flow using nonequilibrium molecular dynamics simulations

C. Baig, B. J. Edwards,[a] D. J. Keffer, and H. D. Cochran
Department of Chemical Engineering, University of Tennessee, Knoxville, Tennessee 37996-2200

V. A. Harmandaris
Max-Planck-Institut for Polymer Research, Theory Group, D-55128 Mainz, Germany

(Received 20 September 2005; accepted 18 January 2006; published online 22 February 2006)

We present various rheological and structural properties of three polyethylene liquids, $C_{50}H_{102}$, $C_{78}H_{158}$, and $C_{128}H_{258}$, using nonequilibrium molecular dynamics simulations of planar elongational flow. All three melts display tension-thinning behavior of both elongational viscosities, η_1 and η_2. This tension thinning appears to follow the power law with respect to the elongation rate, i.e., $\eta \sim \dot{\varepsilon}^b$, where the exponent b is shown to be approximately -0.4 for η_1 and η_2. More specifically, b of η_1 is shown to be slightly larger than that of η_2 and to increase in magnitude with the chain length, while b of η_2 appeared to be independent of the chain length. We also investigated separately the contribution of each mode to the two elongational viscosities. For all three liquids, the intermolecular Lennard-Jones (LJ), intramolecular LJ, and bond-stretching modes make positive contributions to both η_1 and η_2, while the bond-torsional and bond-bending modes make negative contributions to both η_1 and η_2. The contribution of each of the five modes decreases in magnitude with increasing elongation rate. The hydrostatic pressure shows a clear minimum at a certain elongation rate for each liquid, and the elongation rate at which the minimum occurs appears to increase with the chain length. The behavior of the hydrostatic pressure with respect to the elongation rate is shown to correlate with the intermolecular LJ energy from a microscopic viewpoint. On the other hand, $\langle R_{\mathrm{ete}}^2 \rangle$ and $\langle R_g^2 \rangle$ appear to be correlated with the intramolecular LJ energy. The study of the effect of the elongational field on the conformation tensor $\tilde{\mathbf{c}}$ shows that the degree of increase of $\mathrm{tr}(\tilde{\mathbf{c}})-3$ with the elongation rate becomes stronger as the chain length increases. Also, the well-known linear reaction between $\boldsymbol{\sigma}$ and $\tilde{\mathbf{c}}$ does not seem to be satisfactory. It seems that a simple relation between $\boldsymbol{\sigma}$ and $\tilde{\mathbf{c}}$ would not be valid, in general, for arbitrary flows.
 [DOI: 10.1063/1.2174006]

I. INTRODUCTION

During the last few decades, simulations have played a significant role in our understanding of the rheological and structural behaviors of polymeric materials in flowing systems, which is important not only in practical polymer processing but also in advancing our knowledge of the fundamental characteristics of chain molecules, e.g., linear and nonlinear viscoelasticity.'[2] Despite a tremendous advance in computer technology during the last decade, the capability is, however, still not yet enough to make it possible for us to perform simulations of long-chain molecules used in a practical processing operation. However, considering that computational power has increased steadily and rapidly over the recent years, the maximum chain length we can simulate in the future will continue to increase as time goes on. Furthermore, the limit of chain length due to restrictions on computational power is not a complete obstacle in the study of the viscoelasticity of polymers because most fundamental characteristics of the linear and nonlinear viscoelasticity still can be understood from a theoretical point of view using rather short-chain molecules (in a practical sense), i.e., a few hundreds to thousands of carbon atoms for polyethylene solutions or melts. Also, many new efficient methodologies[3,4] have been developed to help simulate long-chain molecules. With all these advances (theory, computational power, and simulation methodology), the role of simulations has become increasingly significant and an essential tool in the study of polymer rheology.

While much understanding of shear flow has been accumulated, not only by actual experiments but also by computer simulations through nonequilibrium molecular dynamics (NEMD) simulations,[5] there have been comparatively few experimental data of elongational flow due to the extreme difficulty in performing these experiments.[2] Furthermore, due to the contraction of at least one dimension with time, NEMD simulations of elongational flow were initially constrained by a limited simulation time, which was easily exceeded by the intrinsic relaxation time of even very short-chain molecules. This difficulty was partially resolved by Kraynik and Reinelt's[6] discovery of the temporal and spatial periodicities of the lattice vectors of a system in a planar

[a]Author to whom correspondence should be addressed. Electronic mail: bjedwards@chem.engr.utk.edu

elongational flow (PEF), and therefore one could, in principle, continue NEMD simulations indefinitely in time. Todd and Daivis[7–10] and Baranyai and Cummings[11] applied these new boundary conditions to NEMD simulations of PEF for simple fluids and demonstrated their usefulness. This work opened up a new dimension for rheological studies: the ability to simulate steady-state planar elongational flow with the same degree of utility as was already possible for steady-state shear flow. The first simulation study by Daivies *et al.*[12] of model polymeric liquids involving both steady-state shear and elongational flows thus became possible, yielding valuable information regarding the rheological characteristic functions in both types of flows.

We have recently performed NEMD simulations of short-chain alkanes, such as $C_{10}H_{22}$ (decane), $C_{16}H_{34}$ (hexadecane), and $C_{24}H_{50}$ (tetracosane) under PEF,[13] extending the work done by Cui *et al.* for steady-state shear flow to steady-state PEF.[14,15] (In the remainder of this article, Ref. 13 will be referred to as "I.") Moreover, we have recently applied these simulation results in PEF, together with those in the shear flow, in assessing several important existing viscoelastic models.[16] We refer readers to previous papers[17,18] for details of the NEMD methodology employed in these simulations.

In this study, we extend our NEMD simulations of PEF from the short-chain alkanes performed in I to the more complex linear polyethylene melts of $C_{50}H_{102}$ up to $C_{128}H_{258}$. This choice of chain lengths should encompass the crossover from the Rouse regime to the reptation regime.[19] As in I for the short-chain alkanes, we again analyze many important rheological properties (such as elongational viscosities) and structural properties (such as the mean square end-to-end distance of chains). In addition, in this work we study separately each contribution of the intermolecular and intramolecular modes to the elongational viscosities. We also investigate the effect of the elongational field on the conformation tensor, which is considered to be an important physical quantity at the coarse-grained level of description.[20,21] The conformation tensor appears to be more reliable than the stress tensor from a statistical viewpoint, since the former is a property averaged over the individual chains in the system, whereas the latter is only a collective property of the entire system. Finally, we briefly look into the relationship between the stress and conformation tensors, and discuss the implications of this relationship with regard to the common linear form of polymer rheology.[20,21]

This paper is organized as follows. In Sec. II, we describe the simulation methodology employed in this work. In Sec. III, we present our simulation results with a detailed analysis from a molecular level, as in I. Finally, we summarize this study in Sec. IV.

II. SIMULATION METHODOLOGY

The *p*-SLLOD equations of motion for *NVT* NEMD simulations using the Nosé-Hoover thermostat[22–24] for arbitrary homogeneous flow are[17]

$$\dot{\mathbf{q}}_{ia} = \frac{\mathbf{p}_{ia}}{m_{ia}} + \mathbf{q}_{ia} \cdot \nabla \mathbf{u},$$

$$\dot{\mathbf{p}}_{ia} = \mathbf{F}_{ia} - \mathbf{p}_{ia} \cdot \nabla \mathbf{u} - m_{ia}\mathbf{q}_{ia} \cdot \nabla \mathbf{u} \cdot \nabla \mathbf{u} - \frac{p_\zeta}{Q}\mathbf{p}_{ia},$$

$$\dot{\zeta} = \frac{p_\zeta}{Q},$$

$$\dot{p}_\zeta = \sum_i \sum_a \frac{\mathbf{p}_{ia}^2}{m_{ia}} - DNk_BT, \tag{1}$$

where $\mathbf{p}_{ia}$, $\mathbf{q}_{ia}$, and $\mathbf{F}_{ia}$ are the momentum, position, and force vectors of atom a in molecule i, of mass m_{ia}.V denotes the volume of the system, N the total number of atoms, T the absolute temperature, and k_B the Boltzmann constant. D denotes dimensionality.ζ and p_ζ are the coordinate- and momentum-like variables of the Nosé-Hoover thermostat, respectively, and $Q=DNk_BT\tau^2$ is the mass parameter of the thermostat. $\nabla\mathbf{u}$ represents the velocity gradient tensor. Note that the term $m_{ia}\mathbf{q}_{ia}\cdot\nabla\mathbf{u}\cdot\nabla\mathbf{u}$ in the momentum equation (1) will vanish for PCF but not for PEF.

The equations of motion were integrated using the reversible reference system propagator algorithm (*r*-RESPA) developed by Tuckerman *et al.*[25] We devised the *r*-RESPA, following the procedure of Tuckerman *et al.*[25] and Cui *et al.*[14] Two time scales are used in the simulations. The larger time step was used for the intermolecular interaction, and the smaller time step for all the intramolecular interactions, such as the bond-stretching, bond-bending, bond-torsional, and intramolecular Lennard-Jones (LJ) interactions. The larger and smaller time steps are 2.26 and 0.226 fs, respectively. The relaxation time parameter τ of the Nosé-Hoover thermostat was set equal to 0.24 ps. As regards the KRBCs, we chose the Hencky strain, $\varepsilon_p \approx 0.9624$, and the initial orientation angle of the simulation box, $\theta_0 \approx 31.718°$, which are obtained by setting $k=3$, $N_{11}=2$, and $N_{12}=-1$ in Ref. 6. The time period t_p for the KRBCs is determined from $\varepsilon_p=\dot{\varepsilon}t_p$. For details, readers are referred to the original paper.[6] For details of the implementation of the *p*-SLLOD algorithm with KRBCs for PEF, we refer readers to Ref. 17.

The potential model employed in this work, which is the same as that in I, was used previously by Cui *et al.*[15] for shear flow. For the sake of completeness, we present this model again here. The model was developed by Siepmann *et al.*[26] and is known as the Siepmann-Karaboni-Smit (SKS) united-atom model, with the exception that the rigid bond is now replaced by a flexible one with a harmonic potential. In this model, the nonbonded intermolecular and intramolecular atom-atom (or site-site) interactions are modeled by the LJ potential,

$$V_{\mathrm{LJ}}(r) = 4\varepsilon_{ij}\left[\left(\frac{\sigma_{ij}}{r}\right)^{12} - \left(\frac{\sigma_{ij}}{r}\right)^{6}\right], \tag{2}$$

where $\varepsilon_{ij}=(\varepsilon_i\varepsilon_j)^{1/2}$ and $\sigma_{ij}=(\sigma_i+\sigma_j)/2$ are the energy and size parameters of the potential between atoms i and j. The parameters ε and σ are chosen as 47 K and 3.93 Å for the CH_2 group, and 114 K and 3.93 Å for the CH_3 group. A cut-off distance of $2.5\sigma_{\mathrm{CH2}}$ was employed in this work. The intramolecular LJ interaction is only active between atoms separated by more than three bonds.

The bond-stretching interaction is modeled by a harmonic potential,

$$V_{\mathrm{str}}(l) = \frac{1}{2} k_{\mathrm{str}} (l - l_{\mathrm{eq}})^2, \tag{3}$$

where the bond-stretching constant $k_{\mathrm{str}}/k_B = 452\,900$ K/Å and the equilibrium length $l_{\mathrm{eq}} = 1.54$ Å. The bond-bending interaction is also governed by a harmonic potential,

$$V_{\mathrm{ben}}(\theta) = \frac{1}{2} k_{\mathrm{ben}} (\theta - \theta_{\mathrm{eq}})^2, \tag{4}$$

where the bond-bending constant $k_{\mathrm{ben}}/k_B = 62\,500$ K/rad^2 and $\theta_{\mathrm{eq}} = 114°$. The torsional interaction is described by the model proposed by Jorgensen *et al.*,[27]

$$V_{\mathrm{tor}}(\phi) = \sum_{m=0}^{3} a_m (\cos\phi)^m, \tag{5}$$

where $a_0/k_B = 1010$ K, $a_1/k_B = 2019$ K, $a_2/k_B = 136.4$ K, and $a_3/k_B = -3165$ K.

The state points for $C_{50}H_{102}$, $C_{78}H_{158}$, and $C_{128}H_{258}$ are as follows: the densities $\rho = 0.7426$ g/cm^3 for $C_{50}H_{102}$, $\rho = 0.7640$ g/cm^3 for $C_{78}H_{158}$, $\rho = 0.7754$ g/cm^3 for $C_{128}H_{258}$, and the same temperature, $T = 450$ K, was used for all three liquids. These densities were chosen based on a previous study by Harmandaris *et al.*[28] Exploring these states by NEMD simulations, we employed 96 molecules (total of 4800 sites) for $C_{50}H_{102}$, 192 molecules (total of 14 946 sites) for $C_{78}H_{158}$, and 416 molecules (total of 53 248 sites) for $C_{128}H_{258}$. These systems, in particular, $C_{128}H_{258}$, were very demanding in computational time, even with the computational power currently available.

We employed these huge systems in order to reduce the system-size effect. Furthermore, we have used a noncubic box for simulations in order to make a larger length for both the x and y dimensions, since these dimensions are contracting and extending with time (after applying the initial orientation angle), and the chains are aligned and extended in those directions. Specifically, the box dimension ($x \times y \times z$ in unit of angstroms) of $65.5 \times 65.5 \times 35.2$ was employed for $C_{50}H_{102}$, $101 \times 101 \times 45.2$ for $C_{78}H_{158}$, and $166 \times 166 \times 58$ for $C_{128}H_{258}$. These box dimensions were chosen based on the fully stretched chain length with the *trans*-conformation of 63.3 Å for $C_{50}H_{102}$, 99.4 Å for $C_{78}H_{158}$, and 164 Å for $C_{128}H_{258}$. However, a non-negligible system-size effect was observed even with these large systems in our preliminary simulations at very high elongation rates, i.e., $\dot{\varepsilon}(m\sigma^2/\varepsilon)^{1/2} \geqslant 0.5$, where the chains were fully elongated to almost the same value of the initial box length in the x or y dimension. Such an undesirable system-size effect restricted the upper limit of elongation rate in this work. By investigating many static and dynamic properties at several high elongation rates for each liquid, the system-size effect was found to be negligible for $\dot{\varepsilon}(m\sigma^2/\varepsilon)^{1/2} \leqslant 0.2$ with the present box dimensions. Therefore, the highest elongation rate used in this study was chosen to be $\dot{\varepsilon}(m\sigma^2/\varepsilon)^{1/2} = 0.2$. On the other hand, this restriction was not considered to be a significant problem, since we still observed the most important nonlinear viscoelastic properties in this range, as will be shown in Sec. III.

We should point out that substantial system-size effects have previously been reported by Morriss *et al.* for $C_{20}H_{42}$ under shear flow.[29] While we have not performed an exhaustive system-size effect study for PEF, we can remark that the effect becomes more dramatic as the field strength increases. Another way to state this is that a box size that is adequate for an equilibrium simulation may very well be inadequate for a nonequilibrium simulation. We performed a system-size analysis sufficient to identify a maximum acceptable elongation rate by comparing systems of N, $4N$, and $9N$ particles for $C_{50}H_{102}$. Above our maximum acceptable elongation rate, we found that steady-state properties, such as the hydrostatic pressure, could differ between simulations of different sizes by more than an order of magnitude; indeed, the system-size effect is dramatic.

Also, note that the maximum accepted elongation rate is still too high of a value for real experiments to achieve at present. More specifically, we used the range of elongation rates $0.001 \leqslant \dot{\varepsilon}(m\sigma^2/\varepsilon)^{1/2} \leqslant 0.2$ for $C_{50}H_{102}$, $0.0002 \leqslant \dot{\varepsilon}(m\sigma^2/\varepsilon)^{1/2} \leqslant 0.2$ for $C_{78}H_{158}$, and $0.0001 \leqslant \dot{\varepsilon}(m\sigma^2/\varepsilon)^{1/2} \leqslant 0.2$ for $C_{128}H_{258}$. The lower limit of elongation rate for each melt is small enough for the system to be in the linear viscoelastic regime, as will be shown in Sec. III.

III. RESULTS AND DISCUSSION

As in I, first, we investigate the two steady-state material functions in planar elongational flow:[2,30] the first elongational viscosity η_1 and the second elongational viscosity η_2, which are defined as

$$\eta_1 = \frac{\sigma_{yy} - \sigma_{xx}}{4\dot{\varepsilon}}, \tag{6a}$$

$$\eta_2 = \frac{\sigma_{yy} - \sigma_{zz}}{2\dot{\varepsilon}}. \tag{6b}$$

Here the extra stress tensor is defined as $\boldsymbol{\sigma} = \boldsymbol{\Pi} - p\boldsymbol{\delta}$, where $\boldsymbol{\Pi}$ denotes the pressure tensor, p the thermodynamic pressure, and $\boldsymbol{\delta}$ the unit tensor. According to the Irving-Kirkwood procedure,[31] the microscopic expression of the pressure tensor $\boldsymbol{\Pi}$ for homogeneous systems is found to be

$$\boldsymbol{\Pi} = \left\langle \frac{1}{V} \sum_i \sum_a \left(\frac{\mathbf{p}_{ia}\mathbf{p}_{ia}}{m_{ia}} + \mathbf{q}_{ia}\mathbf{F}_{ia} \right) \right\rangle, \tag{7}$$

where the angular brackets denote the time average of the system trajectory. The definitions of Eqs. (6) allow for easy comparisons between η_1 and η_2 at low strain rates, since both are equal to each other in the linear (or Newtonian) regime and also to the zero-shear-rate viscosity.

In Fig. 1, η_1 and η_2 are plotted versus the elongation rate for the three polyethylene melts. (The numerical values are presented in Table I.) The vertical lines in the figure represent the "critical elongation rate" $\dot{\varepsilon}_c$, at which the product of a characteristic relaxation time λ and $\dot{\varepsilon}$ (the Weissenberg number[1] $\mathrm{We} \equiv \lambda\dot{\varepsilon}$) is equal to unity and which is often approximately considered the boundary between the linear and nonlinear regimes in flowing systems. The characteristic re-

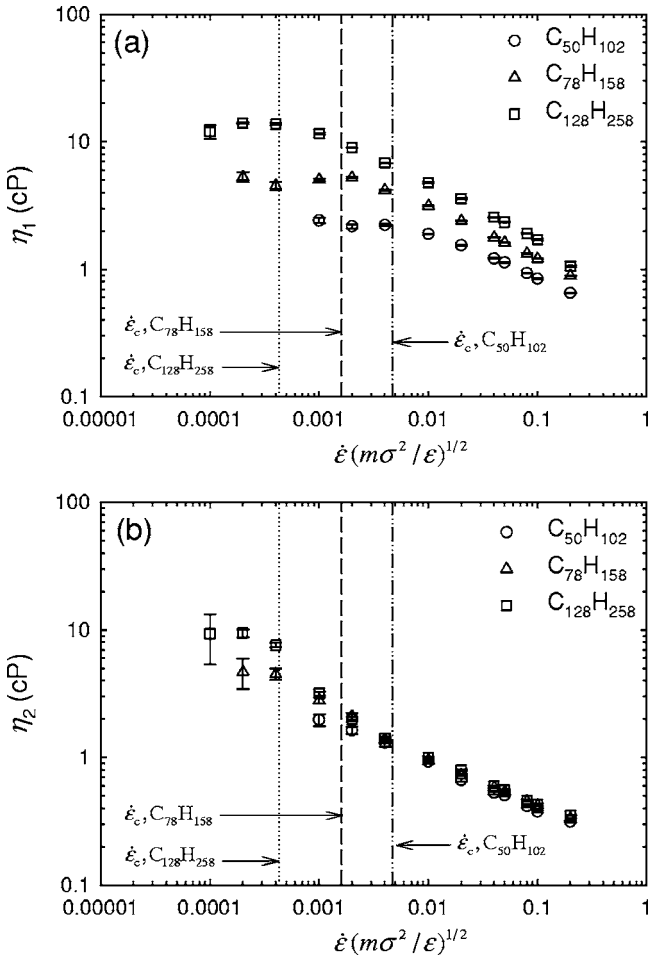

FIG. 1. Comparison of (a) η_1 and (b) η_2 vs the elongation rate between $C_{50}H_{102}$, $C_{78}H_{158}$, and $C_{128}H_{258}$.

laxation time of each system, λ, is commonly regarded as the rotational (longest) relaxation time and can be calculated directly from equilibrium simulations by studying the time correlation function of the chain end-to-end unit vector.[19] Our calculations of λ yield $\lambda=0.5\pm0.03$ ns for $C_{50}H_{102}$, $\lambda=1.45\pm0.15$ ns for $C_{78}H_{158}$, and $\lambda=5.5\pm0.3$ ns for $C_{128}H_{258}$. From these results, the reduced critical elongation rates are found to be $\dot{\varepsilon}_c(m\sigma^2/\varepsilon)^{1/2}\approx0.0047$, 0.0016, and 0.00043 for $C_{50}H_{102}$, $C_{78}H_{158}$, and $C_{128}H_{258}$, respectively.

As shown in Fig. 1, tension-thinning behavior is observed for all three polyethylene melts. Consistent with a well-known fact in polymer physics, both η_1 and η_2 are shown to become larger as the chain length increases. However, for both η_1 and η_2, the difference appears to decrease with increasing elongation rate, which is particularly obvious for η_2. The tension-thinning behavior appears to be more pronounced for the longer chain. Similar to the short-chain alkanes in I, η_1 and η_2 appear not to be equal to each other in general, which indicates that they are indeed two independent material functions in PEF (see Table I). However, as elongation rate decreases, they approach each other and appear to converge well at very low elongation rates, i.e., in the linear regime. This is consistent with the theoretical prediction in the Newtonian limit, using the definitions of Eqs. (6). Based on these results at very low elongation rates, we roughly estimate the Newtonian viscosity μ as $\mu=2.2\pm0.4$ cP for $C_{50}H_{102}$, $\mu=5.0\pm0.8$ cP for $C_{78}H_{158}$, and $\mu=10.7\pm2.8$ cP for $C_{128}H_{258}$.

It would be worth comparing quantitatively the degree of the tension thinning of η_1 and η_2 between the three melts. It is known experimentally that for typical polymeric liquids, the shear thinning of viscosity at high shear rates is well described by a power-law model, such as $\eta_{\text{shear}}\sim\dot{\gamma}^b$, with the exponent b being between -0.4 and -0.9.[1] The calculation based on the above results is that $b=-0.37\pm0.01$ for η_1 and $b=-0.34\pm0.01$ for η_2 of $C_{50}H_{102}$, $b=-0.42\pm0.01$ for η_1 and $b=-0.35\pm0.01$ for η_2 of $C_{78}H_{158}$, and $b=-0.46\pm0.02$ for η_1 and $b=-0.36\pm0.01$ for η_2 of $C_{128}H_{258}$. Therefore, the slopes for the three liquids in PEF appear to be close to the lower limit of the above reported range. We note that the previous study of NEMD simulation of shear flow for $C_{100}H_{202}$ by Moore *et al.*[32] showed that b is approximately -0.35 at high shear rates, which seems to be close to the above values in

TABLE I. Elongational viscosities η_1 and η_2 as functions of elongation rate for $C_{50}H_{102}$, $C_{78}H_{158}$, and $C_{128}H_{258}$. Numbers in parentheses represent the statistical uncertainties in the least significant digits calculated using Eq. (28) of Ref. 27.

	$C_{50}H_{102}$		$C_{78}H_{158}$		$C_{128}H_{258}$	
$\dot{\varepsilon}(m\sigma^2/\varepsilon)^{1/2}$	η_1(cP)	η_2(cP)	η_1(cP)	η_2(cP)	η_1(cP)	η_2(cP)
0.0001					12.0 (15)	9.35 (400)
0.0002			5.31 (45)	4.70 (126)	14.0 (2)	9.42 (73)
0.0004			4.53 (33)	4.50 (45)	13.8 (3)	7.62 (31)
0.001	2.42 (13)	1.97 (21)	5.05 (9)	2.81 (18)	11.6 (1)	3.17 (11)
0.002	2.17 (7)	1.63 (11)	5.24 (6)	2.11 (13)	9.01 (4)	1.99 (8)
0.004	2.23 (4)	1.31 (9)	4.19 (5)	1.38 (5)	6.82 (4)	1.41 (4)
0.01	1.89 (2)	0.927(30)	3.15 (2)	0.947 (18)	4.78 (5)	0.995 (16)
0.02	1.55 (1)	0.666(21)	2.40 (2)	0.729 (13)	3.58 (4)	0.792 (14)
0.04	1.22 (1)	0.528(12)	1.78 (1)	0.586 (7)	2.56 (2)	0.595 (8)
0.05	1.13 (1)	0.505(11)	1.62 (1)	0.539 (7)	2.35 (2)	0.557 (7)
0.08	0.936 (5)	0.416 (6)	1.33 (1)	0.455 (5)	1.91 (1)	0.461 (3)
0.1	0.843 (6)	0.377 (5)	1.21 (1)	0.421 (4)	1.71 (2)	0.429 (4)
0.2	0.654 (4)	0.315 (3)	0.891 (5)	0.333 (2)	1.06 (1)	0.352 (2)

PEF. From these results, it is seen quantitatively that the slope of η_1 increases in magnitude as the chain length increases, but the slope of η_2 does not seem to be sensitive to the chain length. Also, the slope of η_1 appears to be larger than that of η_2, which appears to be more obvious for longer chains.

Daivis *et al.*[12] measured the same elongational viscosities in PEF for a generic polymeric liquid modeled as a bead-rod chain (of variable bead number) using a LJ potential for interactions between the beads. The qualitative behavior found for η_2 in their study is very similar to that described above, except that they observed a tension-thickening behavior at the highest elongation rates, which were not examined in the present study due to system-size effects. For η_1, they observed tension thickening at intermediate elongation rates, in contrast to the behavior described above. Unfortunately, there is not enough experimental data available to assess which result is more reasonable, in particular, for the rather short polyethylene chains simulated in the present work.

We now explore one of the advantages of simulation over real experiments by separately examining the contribution of distinct modes, i.e., intramolecular and intermolecular, to the elongational viscosities. (Note that in the following three figures, the error bars are omitted for a better visual representation.) First, let us look into the kinetic and potential contributions to the viscosities separately. The results are presented in Fig. 2. The kinetic part of the viscosity is shown to be smaller than the potential part by approximately two orders of magnitude. This is, in fact, consistent with the well-known result that the kinetic contribution to the stress tensor is important for gases but not for liquids, for which the potential part is usually dominant. For all three polyethylene liquids, it is evident that the potential part decreases as the elongation rate increases. This offers direct evidence for the tension-thinning behavior of both elongational viscosities. On the other hand, the kinetic part appears to increase consistently with the elongation rate for $C_{50}H_{102}$, but it is not very clear for $C_{78}H_{158}$ and $C_{128}H_{258}$; it still seems to increase with the elongation rate in the intermediate range. However, it should be kept in mind that the kinetic part comprises only a small contribution to the viscosities.

Now let us look into the potential part by separately analyzing the intermolecular LJ and the four intramolecular contributions (bond-stretching, bond-bending, bond-torsional, and intramolecular LJ). In Fig. 3, we present each contribution to η_1 as a function of elongation rate. For all three liquids, the intermolecular LJ, intramolecular LJ, and bond-stretching modes make positive contributions to η_1, while the bond-torsional and bond-bending modes appear to make negative contributions. All five modes appear to decrease in magnitude as the elongation rate increases, except at very low elongation rates. More specifically, the negative contribution of the bond-torsional mode to η_1 seems to be relatively small in magnitude, compared with the bond-bending contribution. Another simple, noticeable feature of Fig. 3 is that the two contributions of the intramolecular LJ and bond-torsional modes appear approximately to cancel out each other over the whole range of the elongation rates. Finally, it is interesting to note from the figure that the biggest contribution in magnitude among all the modes comes from the bond-bending mode. We note that similar results have been observed for η_2.

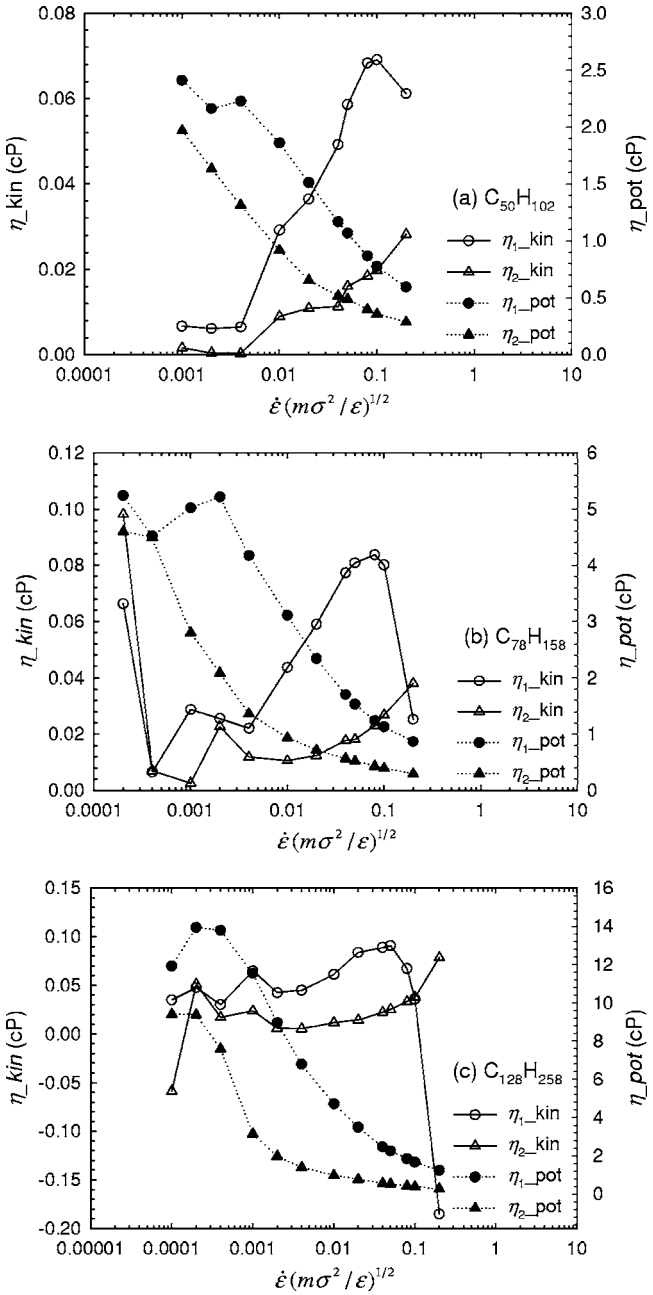

FIG. 2. Kinetic and potential parts of η_1 and η_2 vs the elongation rate for (a) $C_{50}H_{102}$, (b) $C_{78}H_{158}$, and (c) $C_{128}H_{258}$.

Now let us look into another important rheological property. In Fig. 4, the hydrostatic pressure is plotted versus the elongation rate. For all three liquids, the pressure appears to decrease initially with increasing elongation rate, reach a minimum value at an intermediate strain rate, and then increase again after that. This phenomenon was also observed in I for the short-chain alkanes ($C_{10}H_{22}$, $C_{16}H_{34}$, and $C_{24}H_{50}$), where a slight minimum appeared for $C_{16}H_{34}$ and more clearly for $C_{24}H_{50}$. Now, for these longer chains, the minimum is clearly seen in the figure, which thus confirms this behavior in the hydrostatic pressure for long-chain systems. The elongation rate at which the pressure minimum is at-

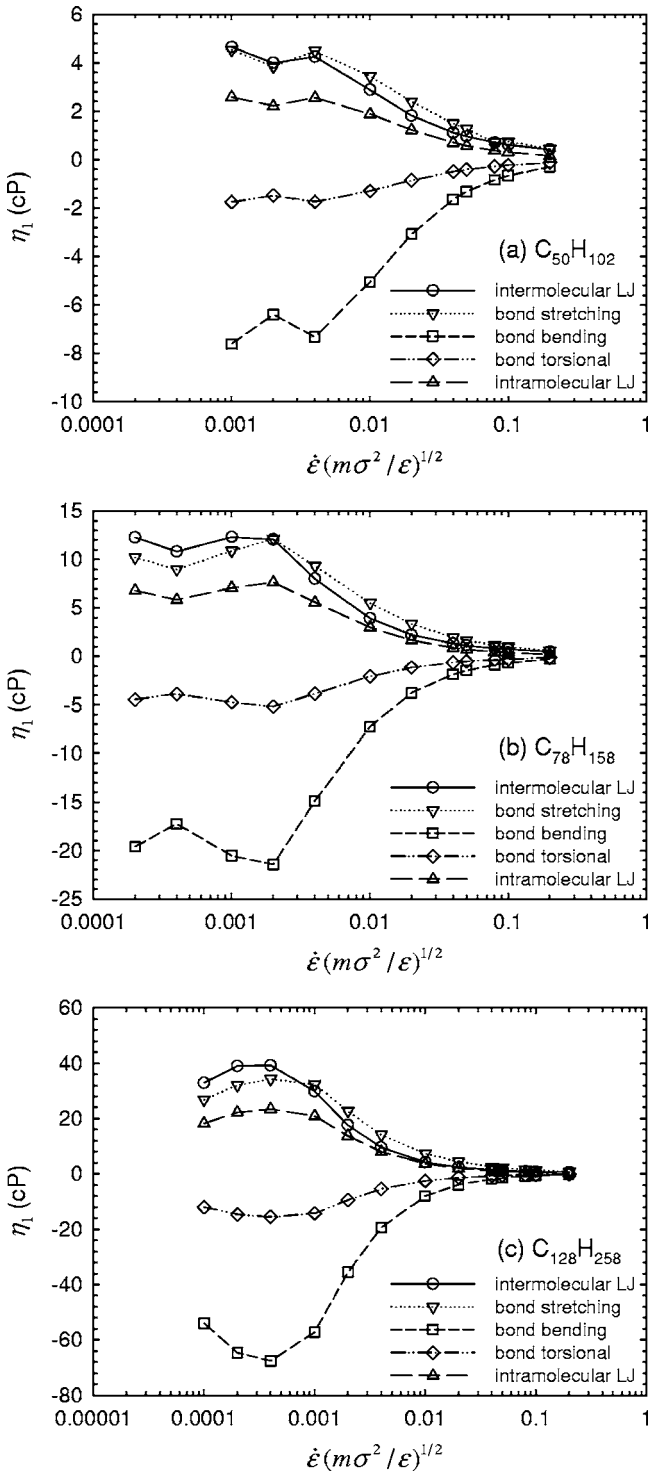

FIG. 3. Contribution of each mode to η_1 as a function of elongation rate for (a) $C_{50}H_{102}$, (b) $C_{78}H_{158}$, and (c) $C_{128}H_{258}$.

tained appears to be approximately $\dot{\varepsilon}(m\sigma^2/\varepsilon)^{1/2} \approx 0.04$ for $C_{50}H_{78}$ and $C_{78}H_{158}$, but slightly higher, $\dot{\varepsilon}(m\sigma^2/\varepsilon)^{1/2} \approx 0.06$, for $C_{128}H_{258}$. It is interesting to compare these values with the value $\dot{\varepsilon}(m\sigma^2/\varepsilon)^{1/2} \approx 0.02$ for $C_{24}H_{50}$. Therefore, it appears that the elongation rate at which the pressure minimum is attained would increase as the chain length increases.

Another interesting point mentioned in I was that the hydrostatic pressure seems to reach a plateau at a very high elongation rate, i.e., $\dot{\varepsilon}(m\sigma^2/\varepsilon)^{1/2} \geqslant 0.8$ for $C_{24}H_{50}$. This phenomenon, however, is not observed in Fig. 4 even with longer chains. This is presumed to be due to a rather low value for the highest elongation rate employed in this work because of the system-size effect at higher elongation rates. Therefore, we still assume that a plateau would be reached at higher elongation rates for all these melts if it were possible to perform the required simulations unambiguously.

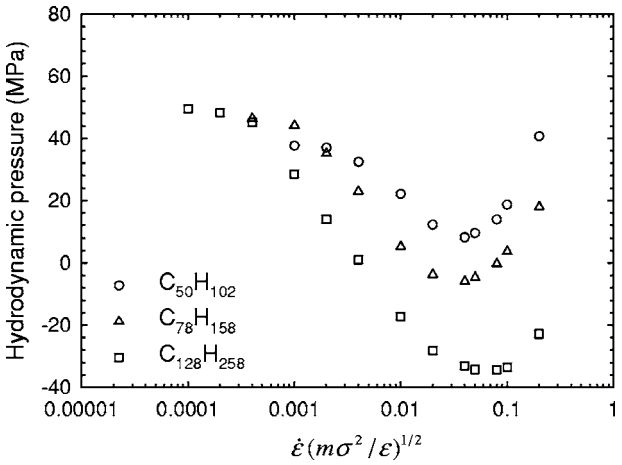

FIG. 4. Hydrostatic pressure vs the elongation rate for $C_{50}H_{102}$, $C_{78}H_{158}$, and $C_{128}H_{258}$. The error bars of all the data are smaller than the size of the symbols.

As shown in I, the above observations for the hydrostatic pressure can be understood from a microscopic viewpoint. The kinetic part of the hydrostatic pressure is already imposed by the temperature, and therefore it is not a function of elongation rate. The potential part is likely to arise mostly from the intermolecular interaction, and therefore it seems to be appropriate to investigate the intermolecular potential energy as a function of elongation rate. The plot of the intermolecular LJ energy versus the elongation rate is shown in Fig. 5. The overall shapes of the plots look very similar to those of the hydrostatic pressure. Also, the minimum observed in the pressure is also observed here. Furthermore, the elongation rate for the intermolecular LJ energy to reach a minimum appears to be very close to that for the hydrostatic

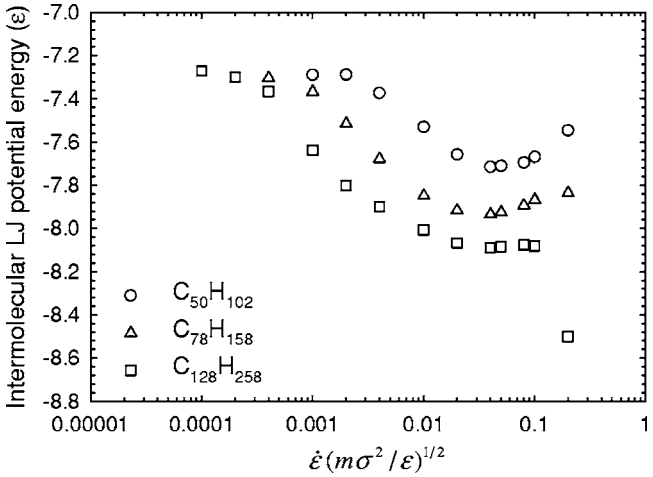

FIG. 5. Intermolecular LJ potential energy per united atom vs the elongation rate for $C_{50}H_{102}$, $C_{78}H_{158}$, and $C_{128}H_{258}$. The error bars of all the data are smaller than the size of the symbols.

pressure for each melt. In Fig. 5, one noticeable difference is observed in $C_{128}H_{258}$, for which the intermolecular LJ energy appears to drop suddenly to a low value at the highest elongation rate. [In fact, a similar phenomenon was observed for $C_{24}H_{50}$ in I at very high elongation rates, $\dot{\varepsilon}(m\sigma^2/\varepsilon)^{1/2}=1.0$.] As in I, all these observations in the intermolecular LJ energy can be explained by considering their molecular origins. We present below those analyses concisely.

In the presence of an elongational field, each molecule will tend to align itself in the direction of the field, resulting in a lowering of the free energy of the system. This alignment of molecules will increase the interaction area between the molecules, and thus result in a decrease of the intermolecular LJ energy, i.e., it becomes more negative. This very plausible physical interpretation explains the decrease of the intermolecular LJ energy with increasing elongation rate initially. However, there is thought to exist another competing effect. The above argument is quite complete only in a static sense. In a dynamic sense, we also need to take into account the molecular collisions between molecules. This effect has been hypothesized by Moore *et al.*[32] in their NEMD simulation work of shear flow with $C_{100}H_{202}$. The molecular collision effect is proposed as a sort of "perturbation" against a static equilibrium configuration of molecules, and therefore is likely to increase the free energy of the system. From a physical point of view, this positive contribution of the molecular collisions to the free energy of the system would become larger with a stronger elongational field, since an elongational field enhances the collisions between molecules. Therefore, the two opposite effects would compete with each other under an elongational flow.

Now let us return to the results of the intermolecular energy in Fig. 5. Initially at low elongation rates, the intermolecular LJ energy decreases with increasing elongation rate due to the effect of the alignment of chains with the field. Meanwhile, however, the effect of the molecular collisions will increase as the elongation rate increases. At a certain elongation rate in this intermediate range, the two effects will compete with each other in magnitude and result in a minimum. A further increase of elongation rate would increase the intermolecular potential energy since the effect of the molecular collisions now becomes more dominant than the alignment effect.

This is still not the whole story. Up to now, we have taken into account the static effect only through the alignment of molecules with the elongational field. However, for very strong elongational fields, it seems that the molecules would not only be aligned along the direction of the field, but also eventually fully stretched out with a zigzag shape, i.e., with the energetically favorable *trans*-conformation along the chain. [This conjecture has been raised in I and will be further considered later in this work; see, for example, Fig. 7(a) below.] This fully stretched conformation of molecules would result in a much larger interaction area between molecules, and thus lower the intermolecular LJ energy.

This effect of the fully stretched conformation of molecules is indeed observed in Fig. 5 for $C_{128}H_{258}$, where the intermolecular LJ energy drops suddenly to a low value at the highest elongation rate. The same effect is not shown in Fig. 5 for $C_{50}H_{102}$ and $C_{78}H_{158}$ because the highest simulated elongation rate for each one is still not large enough to attain the fully stretched state. However, it is very likely that a further increase of the elongation rate would eventually result in such a state, and thus lower the intermolecular LJ energy of each case to a small value. We conjectured in I that this significant structural change would become more pronounced as the chain length increases since the longer chain is likely to be more susceptible to an elongational field. This conjecture can also be verified by directly comparing the elongation rate at which the fully stretched state occurs. According to I, the fully stretched state seems to occur at $\dot{\varepsilon}(m\sigma^2/\varepsilon)^{1/2}\approx 1.0$ for $C_{24}H_{50}$, which is higher than $\dot{\varepsilon}(m\sigma^2/\varepsilon)^{1/2}\approx 0.2$ for $C_{128}H_{258}$. This comparison tells us that such a state would occur for $C_{50}H_{102}$ and $C_{78}H_{158}$ at an elongation rate between these two values. We further suppose that the hydrostatic pressure at the highest elongation rate for $C_{128}H_{258}$ would be a local maximum, i.e., the pressure would be decreased by a further increase of elongation rate. However, we could even further conjecture that at even higher elongation rates, the hydrostatic pressure and the intermolecular LJ energy would increase again with increasing elongation rate because the structural effect would eventually reach its maximum value, with a maximum alignment and the fully stretched conformation at a certain elongation rate. After the maximum, while the conformation is constant, the effect of the molecular collisions would still increase with increasing elongation rate.

Now let us consider the effect of an elongational field on two important structural properties: the mean square end-to-end distance of chains $\langle R_{\mathrm{ete}}^2\rangle$ and the mean square radius of gyration of chains $\langle R_g^2\rangle$. The overall behaviors of $\langle R_{\mathrm{ete}}^2\rangle$ and $\langle R_g^2\rangle$ versus the elongation rate for these melts appear to be very similar to those shown in I for short-chain alkanes. Therefore, in this paper we simply present the numerical values of both $\langle R_{\mathrm{ete}}^2\rangle$ and $\langle R_g^2\rangle$ in Table II and refer readers to the previous paper for plots. As shown in Table II for all three melts, initially both $\langle R_{\mathrm{ete}}^2\rangle$ and $\langle R_g^2\rangle$ appear to increase very rapidly with increasing elongation rate, and then the slope appears to decrease in magnitude at high strain rates. The sudden increase at the initial stage seems to come from the alignment of molecules with the elongational field. However, as mentioned above, a further increase of elongation rate will increase the intermolecular collisions, which are likely to inhibit full molecular elongation. This explains the milder slope at higher strain rates. As mentioned in I, this phenomenon can be better understood by a mean-field concept: a single chain surrounded by a hypothetical field, which exerts numerous random impulses on the chain, would have a smaller extension than its full elongation without the field. In our system, the mean field can be created by the collisions with surrounding molecules. A further increase of elongation rate would make the slope increase, since the chains will be not only more aligned, but also now elongated, to reach eventually a fully stretched state.

This intramolecular structure with respect to the elongation rate can be further understood by investigating the intramolecular LJ energy, which is presented in Fig. 6. As the chains elongate to a greater extent, the favorable intramo-

TABLE II. The mean square end-to-end distance of chains $\langle R_{ete}^2 \rangle$ and the mean square radius of gyration of chains $\langle R_g^2 \rangle$ as functions of elongation rate for $C_{50}H_{102}$, $C_{78}H_{158}$, and $C_{128}H_{258}$. Numbers in parentheses represent the statistical uncertainties in the least significant digits calculated using Eq. (28) of Ref. 27.

	$C_{50}H_{102}$		$C_{78}H_{158}$		$C_{128}H_{258}$	
$\dot{\varepsilon}(m\sigma^2/\varepsilon)^{1/2}$	$\langle R_{ete}^2 \rangle$(Å^2)	$\langle R_g^2 \rangle$(Å^2)	$\langle R_{ete}^2 \rangle$(Å^2)	$\langle R_g^2 \rangle$(Å^2)	$\langle R_{ete}^2 \rangle$(Å^2)	$\langle R_g^2 \rangle$(Å^2)
0	883 (9)	123(1)	1492(25)	218(3)	2 566(20)	389(2)
0.0001					2 729(19)	412(2)
0.0002			1562(28)	224(3)	3 271(15)	466(1)
0.0004			1524(15)	221(2)	4 647(59)	600(6)
0.001	949(10)	128(1)	1922(85)	258(6)	10 996(31)	1116(3)
0.002	957(14)	128(1)	3247(77)	365(5)	14 995(39)	1386(3)
0.004	1247(22)	151(2)	4681(93)	467(5)	17 100(23)	1524(2)
0.01	1825(22)	191(2)	6163(39)	563(3)	18 817(62)	1645(5)
0.02	2286(13)	222(1)	6685(20)	599(1)	19 751(46)	1717(3)
0.04	2536 (9)	238(1)	6955(11)	619(1)	20 404(22)	1772(2)
0.05	2569(13)	240(1)	7017(15)	624(1)	20 627(20)	1792(2)
0.08	2686 (8)	248(1)	7184(13)	637(1)	21 121(15)	1837(1)
0.1	2706 (9)	249(1)	7251(10)	643(1)	21 383(10)	1861(1)
0.2	2801 (7)	256(1)	7602 (9)	674(1)	22 345 (8)	2031(1)

lecular interaction will decrease, which makes the intramolecular LJ energy higher, i.e., less negative, while the elongation results in higher intermolecular interactions, as seen in Fig. 5. A direct comparison between Table II and Fig. 6 shows a close relationship between $\langle R_{ete}^2 \rangle$, $\langle R_g^2 \rangle$, and the intramolecular LJ energy, similar to the relationship between the hydrostatic pressure and the intermolecular LJ energy in Figs. 4 and 5.

The elongated state of the molecules can also be analyzed by investigating the overall chain flexibility, which is mostly governed by the torsional interaction. The bond-torsional energy is plotted versus the elongation rate in Fig. 7(a). Initially, the bond-torsional energy appears to decrease with increasing elongation rate, then reaches a minimum value. After that, it increases further with increasing elongation rate. This phenomenon can also be explained in the same way as above. The initial elongation of molecules with the field makes the bond-torsional energy decrease, i.e., it takes on more of the *trans*-comformation, then reaches a minimum where the intermolecular collisions become strong enough to compete with the alignment effect of the elongated chains. After that, the intermolecular collisions disrupt the stable intramolecular state of the chains. A further increase of elongation rate would eventually make the chains stretch more and more with *trans*-conformations.

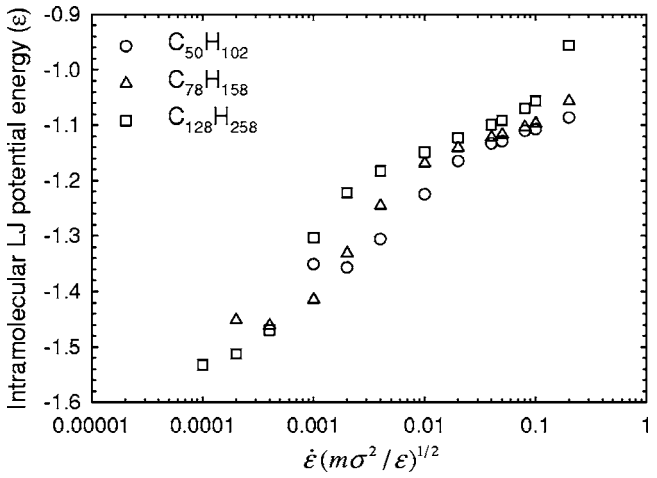

FIG. 6. Intramolecular LJ potential energy per united atom vs the elongation rate for $C_{50}H_{102}$, $C_{78}H_{158}$, and $C_{128}H_{258}$. The error bars of all the data are smaller than the size of the symbols. The number of united atoms in a chain is n for C_nH_{2n+2}.

The comparison between Figs. 6 and 7(a) confirms this hypothesis. Notice in Fig. 7(a) that a plateau appears to be attained for $C_{78}H_{158}$ and $C_{128}H_{258}$, but not yet for $C_{50}H_{102}$. Furthermore, the sudden drop occurring in $C_{128}H_{258}$ at the highest elongation rate, $\dot{\varepsilon}(m\sigma^2/\varepsilon)^{1/2}=0.2$, indicates that chains are going to a fully stretched state, with more *trans*-states. This picture can be better understood by investigating the distribution function with respect to the torsional angle, as shown in I. Instead of showing a similar plot for each melt, here we simply note that the distribution function of the *trans*-state appears to increase initially with the increase of elongation rate until the critical value at which the bond-torsional energy has a minimum. Then, a further increase of elongation rate, which makes the bond-torsional energy higher as shown in Fig. 7(a), makes the distribution function of the *trans*-state smaller. The sudden increase of the *trans*-state for $C_{128}H_{258}$ at $\dot{\varepsilon}(m\sigma^2/\varepsilon)^{1/2}=0.2$ indicates that, in this highly stretched state, the chains seem to be stiff. Although we could not go further to a higher elongation rate due to the system-size effect, as the elongation rate increases further, the chains would get stiffer (higher values of the distribution function of the *trans*-state) and eventually form a crystal-like structure. This is currently a subject of ongoing work conducted by the present authors.[33]

Further study of the chain structure can be carried out by looking into the other two intramolecular modes: the bond-bending and bond-stretching modes. The short-range local chain flexibility would be governed by these two modes. However, note that the contributions of these two modes to $\langle R_{ete}^2 \rangle$ and $\langle R_g^2 \rangle$ usually are very small compared to the contribution of the bond-torsional mode. That is, $\langle R_{ete}^2 \rangle$ and $\langle R_g^2 \rangle$

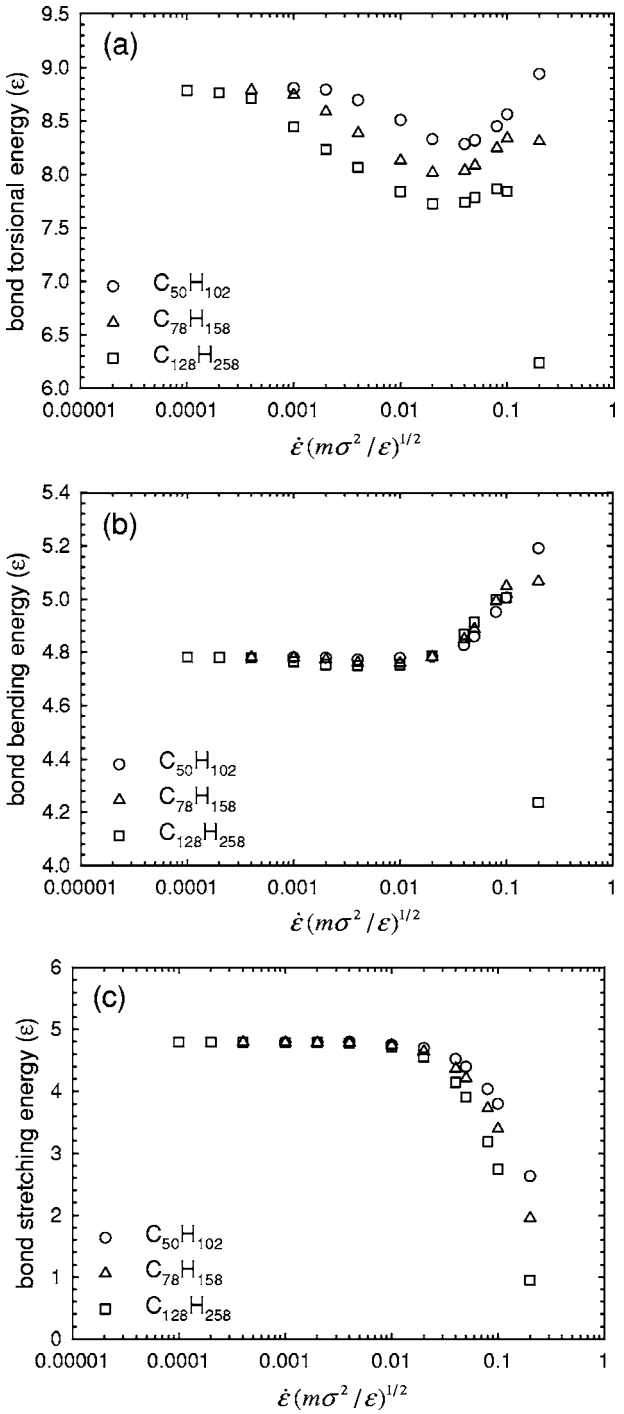

FIG. 7. Plots of (a) bond-torsional energy per mode, (b) bond-bending energy per mode, and (c) bond-stretching energy per mode vs the elongation rate for $C_{50}H_{102}$, $C_{78}H_{158}$, and $C_{128}H_{258}$. The error bars of all the data are smaller than the size of the symbols. The number of torsional modes in a chain is $n-3$ for C_nH_{2n+2}.

are physical quantities governed mostly by the global chain flexibility. The bond-bending energy is shown in Fig. 7(b). The overall shape is qualitatively quite similar to that of the bond-torsional energy, and therefore the same arguments would apply to this phenomenon. However, the minimum appears to be very shallow for all three liquids. This has also been validated by investigating the bond-bending distribution function. Up to the elongation rate at which the minima occur, the distribution functions appear to be independent of the elongation rate. However, further increase of elongation rate increases the bond-bending energy, which is indicated by the broader distribution function with a lower value of the peak for each liquid. As in the case of the bond-torsional energy, a noticeable feature is the sudden increase of the peak in the distribution function at the highest elongation rate in the case of $C_{128}H_{258}$, as can be clearly understood from Fig. 7(b): the shape of the distribution function appears to be narrower with a higher value of the peak. Physically, this means that the bond-bending motion becomes more restricted around the equilibrium angle, and thus the local flexibility of chains is increasingly diminished. Therefore, at the highest elongation rate, the chains of $C_{128}H_{258}$ are stiffer both globally and locally.

Next, let us investigate the bond-stretching mode. The bond-stretching energy is plotted versus the elongation rate in Fig. 7(c). Unlike the bond-torsional and bond-bending energies, the bond-stretching energy appears to decrease monotonically for all three liquids, without any minima or maxima. This seems be due to the strong bond-stretching force for these polyethylene melts. Also, for all the liquids, there seems to be a relatively large drop in the energy at the highest elongation rate. Physically, this means that chains become stiff and more restricted in changing their lengths from the equilibrium value.

This physical behavior can also be understood by investigating again the distribution function. It was observed that the distribution function of the bond-stretching mode clearly becomes narrower with a higher peak as the elongation rate increases. This behavior appears to be more pronounced as the chain length increases. Therefore, the fluctuation of the chain length away from the equilibrium value would be smaller as the elongation rate increases.

Overall, the chains seem to become stiff both locally and globally at high elongation rates. A further increase of elongation rate above the highest value employed in this work would make the chains much stiffer and eventually create a crystal-like structure in the system, where the chains are aligned with the field direction with a fully stretched zigzag shape. Therefore, the system would no longer be isotropic in space. Instead, the aligned direction would be an easier way for the chains to move with their stretched conformation: this movement seems to be a kind of "reptation" and can possibly be described by the reptation model[19] or the Giesekus model.[21]

Next, we investigate the conformation tensor as a function of the elongation rate. The conformation tensor in normalized form is defined as

$$\tilde{\mathbf{c}} = \left\langle \frac{3\mathbf{RR}}{\langle R^2 \rangle_{\mathrm{eq}}} \right\rangle, \tag{8}$$

where $\mathbf{R}$ denotes the end-to-end vector of chain. The angular brackets represent the time average of the system trajectory, and the subscript eq stands for the equilibrium state, at which $\tilde{\mathbf{c}}$ reduces to the unit tensor. Note that in Cartesian coordinates, only the diagonal components of the conformation and stress tensor survive for PEF, and all the other components are equal to zero due to the intrinsic symmetry of the kinematics of the flow.[1,2]

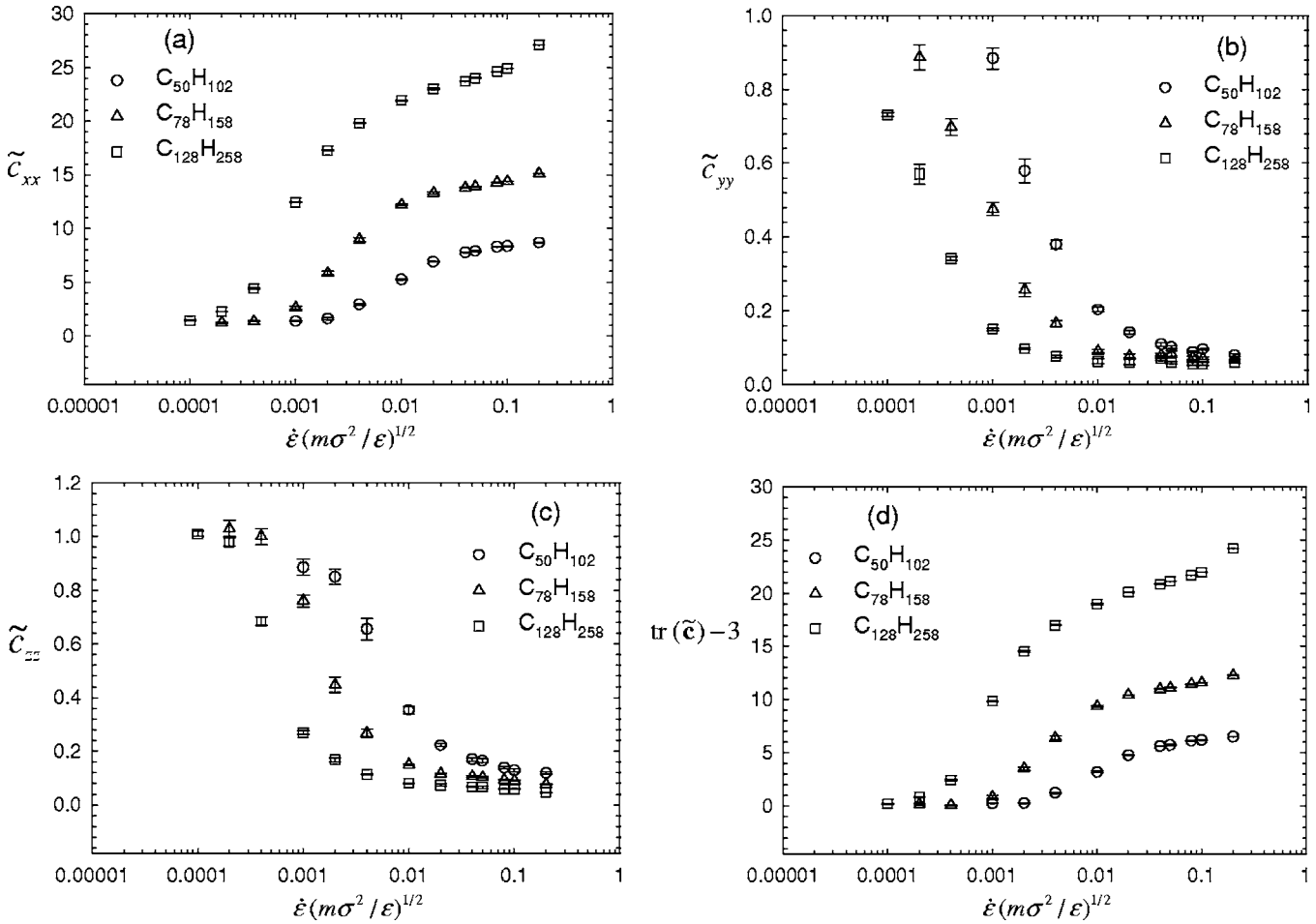

FIG. 8. Conformation tensor vs the elongation rate for $C_{50}H_{102}$, $C_{78}H_{158}$, and $C_{128}H_{258}$; (a) $\tilde{c}_{xx}$, (b) $\tilde{c}_{yy}$, (c) $\tilde{c}_{zz}$, and (d) $\mathrm{tr}(\tilde{\mathbf{c}})-3$.

In Fig. 8, we present the three nonzero components and the trace of $\tilde{\mathbf{c}}$ denoted by $\mathrm{tr}(\tilde{\mathbf{c}})$. As shown in the figure, $\tilde{c}_{xx}$ appears to increase as the elongation rate increases. The slope of $\tilde{c}_{xx}$ appears to be large initially and decreases as the elongation rate increases. This behavior can be explained by the two competing effects that we already mentioned before. On the contrary, both $\tilde{c}_{yy}$ and $\tilde{c}_{zz}$ are shown to decrease, and more specifically, $\tilde{c}_{yy}$ decreases more than $\tilde{c}_{zz}$, which is physically reasonable considering the kinematics: the x dimension elongates, the y dimension contracts, and the z dimension is neutral. However, due to the chain alignment in the x direction, $\tilde{c}_{zz}$ still decreases as the elongation rate increases. In Fig. 8(d), we plot $\mathrm{tr}(\tilde{\mathbf{c}})-3$ as a function of elongation rate. As expected, $\mathrm{tr}(\tilde{\mathbf{c}})-3$ increases with the elongation rate. This increase appears to be larger as the chain length increases. [Notice from Eq. (8) that $\mathrm{tr}(\tilde{\mathbf{c}})-3$ is equal to zero at equilibrium.]

Next, we investigate the relationship between the extra stress tensor $\boldsymbol{\sigma}$ and the conformation tensor. There exists a common linear relationship between $\boldsymbol{\sigma}$ and $\tilde{\mathbf{c}}$ in polymer rheology,[20,21]

$$\sigma_{\alpha\beta} = -nk_BT(\tilde{c}_{\alpha\beta} - \delta_{\alpha\beta}). \tag{9}$$

In terms of the reduced units that are useful in simulations, Eq. (9) can be written as

$$\sigma^*_{\alpha\beta} = -n^*T^*(\tilde{c}_{\alpha\beta} - \delta_{\alpha\beta}), \tag{10}$$

where $T^* = k_BT/\varepsilon$, $\sigma^*_{\alpha\beta} = \sigma_{\alpha\beta}/(\varepsilon/\sigma^3_{\mathrm{CH_2}})$, and $n^* = n\sigma^3_{\mathrm{CH_2}}$. This linear equation originally came from the theory of rubber elasticity, assuming affine deformation of solid rubber, and can also easily be derived for polymer solutions or melts, assuming the Gaussian chain approximation for the end-to-end vector of chains or chain segments. The stress tensor in Eq. (9) is, in fact, only concerned with the intramolecular entropic force. (It does not take into account any other entropic effects due to the intermolecular anisotropy in space, which may become important at high field strength in some flows.)

In Fig. 9, we present three plots. The plots of $\tilde{c}_{zz} - \tilde{c}_{yy}$ and $\tilde{c}_{xx} - \tilde{c}_{yy}$ in the figure directly verify that the linear relation in Eq. (9) is not valid, in general. Moreover, the shapes of the two plots look very different from each other. Therefore, a simple relation between $\boldsymbol{\sigma}$ and $\tilde{\mathbf{c}}$ would not be valid in general for arbitrary flows. This fact may be further supported by the comparison between $\mathrm{tr}(\tilde{\mathbf{c}})$ and $\mathrm{tr}(\boldsymbol{\Pi})$, as shown in Fig. 9(c). Notice that the hydrostatic pressure is calculated by $\mathrm{tr}(\boldsymbol{\Pi})/3$, so that Fig. 9(c) can be readily understood from Figs. 4 and 8(d).

IV. CONCLUSIONS

In this work, we investigated various rheological and structural properties for three polyethylene liquids ($C_{50}H_{102}$,

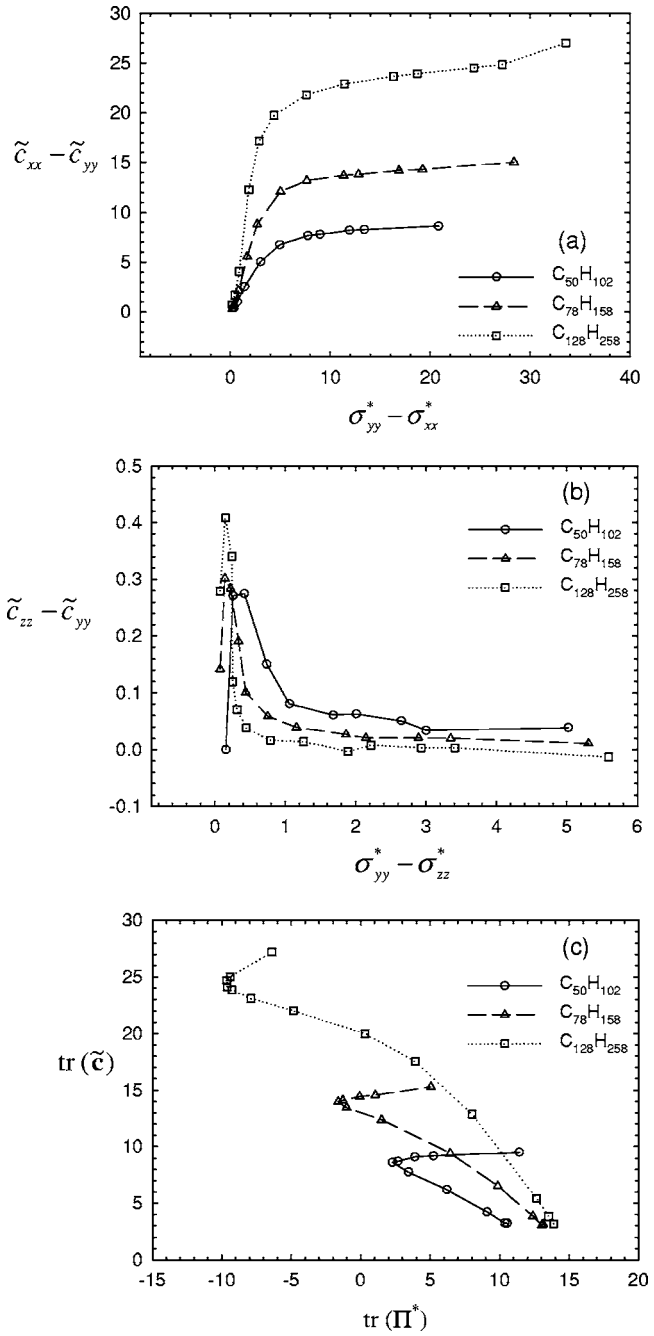

FIG. 9. Relationship between the conformation and the stress tensors; (a) $\tilde{c}_{xx}-\tilde{c}_{yy}$ and $\sigma^*_{yy}-\sigma^*_{xx}$, (b) $\tilde{c}_{zz}-\tilde{c}_{yy}$ and $\sigma^*_{yy}-\sigma^*_{zz}$, and (c) $\mathrm{tr}(\tilde{\mathbf{c}})$ and $\mathrm{tr}(\mathbf{\Pi}^*)$.

$C_{78}H_{158}$, and $C_{128}H_{258}$) using NEMD simulations of PEF. Many physical properties for these rather long chains appeared to be qualitatively similar to those for shorter chains in I. The tension-thinning behaviors of η_1 and η_2 were observed for all three melts and appeared to follow the conventional power-law model of shear flow. The exponent of the power law appeared to be approximately −0.4 for η_1 and η_2. More specifically, the exponent of η_1 was shown to be a little larger than that of η_2 and increased in magnitude with the chain length, while the exponent of η_2 appeared to be independent of the chain length. Also, for all three liquids, the intermolecular LJ, intramolecular LJ, and bond-stretching modes made positive contributions to both η_1 and η_2, while the bond-torsional and bond-bending modes made negative contributions to both η_1 and η_2. The contribution of each of the five modes decreased in magnitude with increasing elongation rate.

The hydrostatic pressure showed a minimum at a certain elongation rate for each liquid, and the elongation rate at which the minimum occurred appeared to increase with the chain length. The behavior of the hydrostatic pressure with respect to the elongation rate could be understood by investigating the intermolecular LJ energy from a microscopic viewpoint. On the other hand, the behavior of $\langle R^2_{\mathrm{ete}}\rangle$ and $\langle R^2_g\rangle$ with respect to the elongation rate appeared to be correlated with the intramolecular LJ energy. A noticeable feature was that $C_{128}H_{258}$ appeared to have a highly stretched conformation at the highest elongation rate, $\dot{\varepsilon}(m\sigma^2/\varepsilon)^{1/2}=0.2$, at which a sudden drop was observed in the intermolecular LJ, bond-bending, and bond-torsional energies. The bond-torsional, bond-bending, and bond-stretching energies could be understood through the investigation of the distribution function of each mode.

Lastly, regarding the conformation tensor, the degree of the increase of $\mathrm{tr}(\tilde{\mathbf{c}})-3$ with the elongation rate appeared to be stronger as the chain length increased. Also, the common linear relation between $\boldsymbol{\sigma}$ and $\tilde{\mathbf{c}}$ did not appear to be satisfactory. Furthermore, there did not seem to exist a simple relation between $\boldsymbol{\sigma}$ and $\tilde{\mathbf{c}}$ that would be valid, in general, for an arbitrary flow field.

This work with longer chains has revealed a promising potential for a future work with much longer chains. This is important since there seems to be a possibility in combining the present methodology of NEMD simulations of PEF and recently developed efficient Monte Carlo methodology[3,4] to make it possible to investigate very long chains, i.e., molecules larger than $C_{500}H_{1002}$.

ACKNOWLEDGMENTS

We would like to acknowledge helpful correspondence with Dr. V. G. Mavrantzas in the preparation of this work. This research was supported by the Division of Materials Sciences and Engineering of the U.S. Department of Energy (DOE) at Oak Ridge National Laboratory (ORNL) through a subcontract at the University of Tennessee. This research used resources of the Center for Computational Sciences at Oak Ridge National Laboratory, which is supported by the Office of Science of the DOE also under Contract No. DE-AC05-00OR22725.

[1] R. B. Bird, R. C. Armstrong, and O. Hassager, *Dynamics of Polymeric Liquids*, Fluid Mechanics Vol. 1, 2nd ed. (Wiley-Interscience, New York, 1987).
[2] F. A. Morrison, *Understanding Rheology* (Oxford University Press, New York, 2001).
[3] V. G. Mavrantzas and D. N. Theodorou, Macromolecules **31**, 6310 (1998).
[4] N. C. Karayiannis, V. G. Mavrantzas, and D. N. Theodorou, Phys. Rev. Lett. **88**, 105503 (2002).
[5] D. J. Evans and G. P. Morriss, *Statistical Mechanics of Nonequilibrium Liquids* (Academic, New York, 1990).
[6] A. M. Kraynik and D. A. Reinelt, Int. J. Multiphase Flow **18**, 1045 (1992).
[7] B. D. Todd and P. J. Daivis, Phys. Rev. Lett. **81**, 1118 (1998).
[8] B. D. Todd and P. J. Daivis, Comput. Phys. Commun. **117**, 191 (1999).
[9] B. D. Todd and P. J. Daivis, J. Chem. Phys. **112**, 40 (2000).

[10] B. D. Todd, Comput. Phys. Commun. **142**, 14 (2001).
[11] A. Baranyai and P. T. Cummings, J. Chem. Phys. **110**, 42 (1999).
[12] P. J. Daivis, M. L. Matin, and B. D. Todd, J. Non-Newtonian Fluid Mech. **111**, 1 (2003).
[13] C. Baig, B. J. Edwards, D. J. Keffer, and H. D. Cochran, J. Chem. Phys. **122**, 184906 (2005).
[14] S. T. Cui, P. T. Cummings, and H. D. Cochran, J. Chem. Phys. **104**, 255 (1996).
[15] S. T. Cui, S. A. Gupta, P. T. Cummings, and H. D. Cochran, J. Chem. Phys. **105**, 1214 (1996).
[16] C. Baig, Ph.D. dissertation, University of Tennessee, 2005.
[17] C. Baig, B. J. Edwards, D. J. Keffer, and H. D. Cochran, J. Chem. Phys. **122**, 114103 (2005).
[18] B. J. Edwards, C. Baig, and D. J. Keffer, J. Chem. Phys. **123**, 114106 (2005).
[19] M. Doi and S. F. Edwards, *The Theory of Polymer Dynamics* (Oxford University Press, New York, 1986).
[20] R. B. Bird, C. F. Curtiss, R. C. Armstrong, and O. Hassager, *Dynamics of Polymeric Liquids*, Kinetic Theory, Vol. 2. 2nd ed. (Wiley-Interscience, New York, 1987).
[21] A. N. Beris and B. J. Edwards, *Thermodynamics of Flowing Systems* (Oxford University Press, New York, 1994).
[22] S. Nosé, Mol. Phys. **52**, 255 (1984).
[23] S. Nosé, J. Chem. Phys. **81**, 511 (1984).
[24] W. G. Hoover, Phys. Rev. A **31**, 1695 (1985).
[25] M. Tuckerman, B. J. Berne, and G. J. Martyna, J. Chem. Phys. **97**, 1990 (1992).
[26] J. I. Siepmann, S. Karaborni, and B. Smit, Nature (London) **365**, 330 (1993).
[27] W. L. Jorgensen, J. D. Madura, and C. J. Swenson, J. Am. Chem. Soc. **106**, 6638 (1984).
[28] V. A. Harmandaris, V. G. Mavrantzas, D. N. Theodorou, M. Kröger, J. Ramiraz, H. C. Öttinger, and D. Vlassopoulos, Macromolecules **36**, 1376 (2003).
[29] G. P. Morriss, P. J. Daivis, and D. J. Evans, J. Chem. Phys. **94**, 7420 (1991).
[30] P. Hachmann and J. Meissner, J. Rheol. **47**, 989 (2003).
[31] J. H. Irving and J. G. Kirkwood, J. Chem. Phys. **18**, 817 (1950).
[32] J. D. Moore, S. T. Cui, H. D. Cochran, and P. T. Cummings, J. Non-Newtonian Fluid Mech. **93**, 83 (2000).
[33] T. Ionescu, C. Baig, B. J. Edwards, D. J. Keffer, and A. Habenschuss, Phys. Rev. Lett. **96**, 037802 (2006).